Applied Physics Letters

RESEARCH ARTICLE | NOVEMBER 14 2022

A promising outlook on the development of lead halide perovskites as spin-orbitronic materials

A. Filippetti ; P. Wadhwa ; C. Caddeo ; A. Mattoni

Appl. Phys. Lett. 121, 200501 (2022)
https://doi.org/10.1063/5.0107903

Applied Physics Letters PERSPECTIVE scitation.org/journal/apl

A promising outlook on the development of lead halide perovskites as spin-orbitronic materials

Cite as: Appl. Phys. Lett. **121**, 200501 (2022); doi: 10.1063/5.0107903
Submitted: 7 July 2022 · Accepted: 5 October 2022 ·
Published Online: 14 November 2022

A. Filippetti,[1,2,a] P. Wadhwa,[1] C. Caddeo,[2] and A. Mattoni[2]

AFFILIATIONS

[1]Dipartimento di Fisica, Università di Cagliari, Cittadella Universitaria, S. P. Monserrato-Sestu Km.0, 700, Monserrato 09042-I, CA, Italy
[2]Consiglio Nazionale delle Ricerche, Istituto Officina dei Materiali, CNR-IOM Cagliari, Cittadella Universitaria, Monserrato 09042-I, CA, Italy

[a)]Author to whom correspondence should be addressed: alessio.filippetti@dsf.unica.it

ABSTRACT

Hybrid lead halide perovskites have progressively overcome the horizon of materials for novel, highly efficient solar cells and are now proposed for a variety of optoelectronic, nanoelectronic, and thermoelectric applications. In this Perspective, we focus on a still scarcely explored and yet extremely thrilling playground: the use of lead halide perovskites to design efficient magneto-electronic and magneto-optic applications. Our analysis is pointed to emphasize the unique combination of strong spin–orbit coupling and wide structural and chemical flexibility, which characterize the lead halide perovskites. Using model calculations, we furnish a qualitative evidence of their capabilities for what concerns the charge–spin conversion mechanism, which is basic to some of the most visionary spin-orbitronic implementations, such as the magnetoelectric switching and the spin-diffusive transistor.

I. INTRODUCTION

Out of the many amazing properties attributed to hybrid lead halide perovskites (HPs), a very special place should be reserved to the Rashba effect (RE),[1–3] perhaps the most fascinating and elusive at the same time. The large spin–orbit coupling (SOC) of Pb and, on a minor extent, of I or Br, together with the dominant presence of these atoms at the bandgap extrema, set up the perfect scenario to convey an extra-large Rashba splitting at both conduction and valence bands, as theoretically predicted by *ab initio* calculations and models.[4–12] Interest for the RE in HPs was initially addressed to explore the hypothesis of an indirect bandgap, which could suppress or reduce the electron–hole recombination.[13–16] This hypothesis was found in contrast with several photoemission measurements[17,18] showing that the recombination rate become faster with decreasing temperature, as it should be in direct bandgap materials. It is important to point out, however, that this observation does not imply the absence of RE at all: according to calculations, in HPs, the RE occurs at both the conduction band bottom (CBB) and the valence band top (VBT), with a k-space offset ~ 0.01 Å^{-1}; this corresponds to a direct–indirect bandgap difference as small as a few meV; furthermore, the direct optical transition between VBT and CBB energies is allowed by the spin orientation. Thus, the residual bandgap indirectness is probably scarcely relevant in optical measurements, except, perhaps, at very low temperature. In fact, *ab initio* calculations show that the radiative recombination rate for $MAPbI_3$ is reduced due to the RE by less than a factor 2.[10,11] In our opinion, these results show that the RE is hardly a key factor in the peculiar photoconversion properties of HPs.

More fundamentally, the very same presence of RE in HPs has been intensely debated in the last few years. In fact, the peculiar dynamics associated with the molecular sublattice makes HPs a case study of the outmost complexity for what concerns electric polarization and RE, two interlaced phenomena that depend on the detail of the atomic structure. To rationalize this complexity, in the literature, a distinction is made between *static* RE and *dynamic* RE: the former is derived by static, built-in dipole fields that may occur in a number of situations: genuinely polarized low-temperature surfaces,[19] ferroelastic nanodomains,[20] nanocrystals,[21,22] 2D perovskites,[23–28] heterostructures,[29,30] perovskite quantum-dots,[31] and doped perovskites.[32] The dynamical RE[6,14] explores the possibility that even in a globally centrosymmetric phase, which is believed to represent the HPs at room temperature, the RE can still show up, due to correlated molecular fluctuations, albeit on short length-scale (∼nm) and timescale (∼ps). An overview of the literature on the topic is given in Sec. III.

The main objective of this work is shading light on the perspectives that HPs may have for future spin-orbitronic nanotechnology. In fact, the exciting aspect of RE in HPs, whether or not sizeable at room

temperature, resides in its large tunability by structural, chemical, and electrical engineering: at the structural level, a large stream of work is nowadays focused on alternative stoichiometries, such as 2D layered perovskites and cation-mixed double perovskites; in layered perovskites, the RE can be enhanced by the natural presence of dipole fields in the charge-confined direction;[27] the double perovskites, on the other hand, are eagerly investigated as possible solutions for Pb replacement, and the variety of allowed chemical combinations opens up a vast landscape for materials design with enhanced properties, including magnetism.[33,34] For what concerns electrical manipulation, there is consensus nowadays on the fact that 3D hybrid perovskites are not ferroelectric, at least at room temperature; nevertheless, poling can induce metastable, long-living polar structures in specific directions (the "electrect" states)[20] where a large RE could be designed. The possibility to modulate and control the amplitude of RE is the key ingredient to envision robust, spin–orbit based magnetoelectric (ME) coupling mechanisms.

Remarkably, while the RE is an old discovery of the 60s, its appeal in the materials science community has been skyrocketing in the last 10 years.[35–39] The intriguing aspect of RE stems from the fact that electrons (and holes) split their energies according to their up- or down-spin orientation, but the energy splitting is swapped by reverting the sign of the electron crystalline momentum (i.e., the band velocity); this feature, called the time-reversal symmetry, constrains the electrons to carry zero net magnetization in real space, with the spin-splitting only occurring in k-space. This fosters a possible route to couple electron spin and current, which, on the other hand, is way more problematic to achieve in magnetic materials by "traditional" spintronic means. A whole new research area, the "spin-orbitronics," was coined and is nowadays flourishing, based on the idea that it is possible to manipulate spin–orbit coupling by electric, magnetic, strain, or even radiative fields, in turn fostering visionary applications, such as electrically controlled magnetic switching,[35–37] quantum devices based on topological properties,[38,39] spin diffusive transistors,[40] and 1D nanowires with Majorana modes.[41,42] The exploitation of HPs for spin-orbitronics has been proposed in few works,[43,44] and the possibility of photoinduced magnetization and ultrafast spin-optic manipulation in HPs has been demonstrated.[45–50] Here, we start from the paradigmatic lead-halide perovskite $MAPbI_3$ as prototype material and discuss the perspective of HPs for charge–spin conversion induced by strong Rashba coupling. This mechanism, called the Rashba–Edelstein effect (REE)[51] or inverse spin-galvanic effect, should not be confused with the spin-Hall effect (SHE),[52,53] which in several interesting systems (e.g., topological semimetals and topological insulators) may occur simultaneously to REE. The SHE is phenomenologically similar but conceptually different from the REE and will not be discussed in this work.

II. FUNDAMENTALS OF RASHBA SPLITTING IN $MAPbI_3$

An electron moving in an electric field $\boldsymbol{E}$ experiences in its rest frame an effective, spin–orbit (SO) magnetic field orthogonal to both the electron velocity and the electric field,

$$\mathbf{B}_{so} = \frac{1}{c^2}\mathbf{E}\times\mathbf{v}. \tag{1}$$

At the atomic level, the internal electric field is provided by the attractive interaction between the electron and the respective ion-core, but in non-centrosymmetric materials, additional contributions come from local dipole fields. The SO magnetic field interacts with the spin momentum of the electron itself, causing the spin-splitting of the bands in k space. Some qualitative insight on the spin-splitting mechanism is furnished by the Zeeman-like modeling of the SOC energy; assuming the Landé factor equal to 2, we can write

$$\Delta\varepsilon_{SO} = -\mathbf{B}_{so}\cdot\boldsymbol{\mu}_s = \mathbf{B}_{so}\cdot\mu_B\boldsymbol{\sigma} = \frac{\mu_B}{c^2}(\mathbf{E}\times\mathbf{v})\cdot\boldsymbol{\sigma}, \tag{2}$$

where $\boldsymbol{\sigma}$ is the spin versor; the spitting lowers the energy of the electrons with spin aligned to $\boldsymbol{B}_{so}$ with respect to that with opposite spin; if the velocity is reversed, $\boldsymbol{B}_{so}$ and $\Delta\varepsilon_{SO}$ are also reversed, i.e., the SO energy is odd in the electron velocity: $\Delta\varepsilon_{SO}(\mathbf{v}) = -\Delta\varepsilon_{SO}(-\mathbf{v})$. From this feature, two important consequences follow: (a) the splitting preserves time reversal symmetry $\varepsilon^{\uparrow}(\mathbf{k}) = \varepsilon^{\downarrow}(-\mathbf{k})$; and (b) a non-vanishing splitting requires $\varepsilon^{\uparrow}(\mathbf{k}) \neq \varepsilon^{\uparrow}(-\mathbf{k})$ for both spin channels, i.e., inversion symmetry must be broken.

The amplitude of SO spitting and the related spin texture are strongly material-dependent; however, two peculiar SOC models are more usually featured in crystals: the Dresselhaus effect (DE)[54] in non-centrosymmetric, non-polar systems (e.g., zinc blende materials), and the RE in non-centrosymmetric systems characterized by a unique polar axis; eventually, non-centrosymmetric materials can display a mixture of DE and RE. From technological viewpoint, the RE is the most attractive for its potential exploitation in electromagnetic applications where the spin can be controlled by electric fields and vice versa. Assuming a dipole field along, say, the z axis, and band velocities in the effective mass approximation, the resulting energy splitting is linearly dependent on the crystalline momentum,

$$\Delta\varepsilon_{SO} = \frac{\mu_B\hbar\mathcal{E}}{m^*c^2}(\hat{\mathbf{z}}\times\mathbf{k})\cdot\boldsymbol{\sigma} = \alpha(\hat{\mathbf{z}}\times\mathbf{k})\cdot\boldsymbol{\sigma}, \tag{3}$$

where α is called the Rashba coefficient; accordingly, near the CBB, the electron energies are

$$\varepsilon_{\boldsymbol{\sigma}}(\mathbf{k}) = \frac{\hbar^2k^2}{2m^*} + \alpha(\hat{\mathbf{z}}\times\mathbf{k})\cdot\boldsymbol{\sigma} = \frac{\hbar^2k^2}{2m^*} + \alpha\left(k_x\sigma_y - k_y\sigma_x\right), \tag{4}$$

where spin-momentum locking forces the spin to be normal to the crystalline momentum; this leaves two possible solutions for the Rashba model: a clockwise (c) band, with spin rotating clockwise around the Fermi contour, and an anticlockwise (a) band; the corresponding spins are

$$\boldsymbol{\sigma}_{c,a}(\mathbf{k}) = \frac{1}{k_p}\begin{pmatrix}\pm k_y\\ \mp k_x\end{pmatrix}, \tag{5}$$

where $k_p = \sqrt{k_x^2 + k_y^2}$; the upper and lower signs are associated with c and a bands, respectively. By substituting this result in the electronic energy, we obtain the following equation for the conduction bands:

$$\varepsilon_{c,a}(\mathbf{k}) = \frac{\hbar^2k^2}{2m^*} \mp \alpha k_p, \tag{6}$$

and thus the c band is the lowest in energy. From Eq. (6), we can extract α in terms of the splitting energy to k-space shift ratio

$$\alpha = \frac{\varepsilon_a(\mathbf{k}) - \varepsilon_c(\mathbf{k})}{2k_p}. \tag{7}$$

Analogously, for the valence bands

$$\varepsilon_{c,a}(\mathbf{k}) = -\frac{\hbar^2 k^2}{2m^*} \pm \alpha k_p; \quad \alpha = \frac{\varepsilon_c(\mathbf{k}) - \varepsilon_a(\mathbf{k})}{2k_p}. \tag{8}$$

The *ab initio* calculated band energies of MAPI display a remarkable similarity with the model of Eqs. (6)–(8). In Fig. 1,[12] we see the results from one of the many *ab initio* calculations present in the literature (they are all qualitatively similar). This band structure is for the energy lowest, static atomic structure of $MAPbI_3$; the presence of RE implies that this is a polar structure with a polarization axis and a dipole field in the direction perpendicular to the Rashba splitting plane. At each k point, the SOC-free spin-degenerate band splits in two chiral bands (c and a, depicted in red and blue, respectively) having opposite spins. Spins are bigger for the valence bands that are mainly contributed by Pb 6s states, whose angular momentum is entirely determined by the spin; on the other hand, the conduction bands derive from Pb 6p states, and thus a large portion comes from the orbital part. Also, due to the Rashba splitting, CBB and VBT are not single points in k-space: they draw rings of radius Δk in the plane perpendicular to the dipole field.

If we define $\Delta\varepsilon$ as the band splitting energy at the band extrema, the Rashba coefficient is $\alpha = \Delta\varepsilon/(2\Delta k)$. For the calculation shown in Fig. 1, we obtain $\Delta k \sim 2.2 \times 10^{-2}$ Å^{-1} and $\alpha \sim 1.2$ eVÅ for the conduction bands, and $\Delta k \sim 1.8 \times 10^{-2}$ Å^{-1} and $\alpha \sim 0.7$ eVÅ for the valence bands. An equivalent expression is $\alpha = 2\varepsilon_0/\Delta k$, where ε_0 is the difference between the band extrema and the band crossing point at Γ; in Fig. 1, $\varepsilon_0 \sim 30$ meV for the CBB and ~ 20 meV for the VBT. The sum of these two ε_0 values gives the bandgap decrease caused by the RE; the value of Δk is easily calculated from $\partial\varepsilon_c(\mathbf{k})/\partial k_p = 0$:

$$\Delta k = \frac{m^*}{\hbar^2}\alpha. \tag{9}$$

It is worth noticing that the dipole field, which generates the Rashba splitting ($\sim 10^7$ V/cm),[12] is similar to those found in typical 2D polar heterostructures.[55] Using this electric field value in Eq. (3), we obtain a Rashba coefficient $\alpha \sim 10^{-6}$ eVÅ, which is, thus, 6 orders of magnitude lower than those actually calculated from the band structure. Such a huge discrepancy indicates that the Zeeman-like model is only valid at qualitative level: the SOC operator exerts a strong action on the electronic wavefunctions which is completely unaccounted by the model. In other words, the linear parametrization of Eq. (6) is valid provided that α is extracted by *ab initio* band structure calculations.

We remark that $\alpha \sim$ eVÅ is quite a large value for a 3D bulk system, and it classifies $MAPbI_3$ in the league of strong Rashba materials; to name a few of them, at the top of the line we have the heavy-metal bulk semiconductor BiTeI ($\alpha = 3.8$ eVÅ),[56] the bulk semimetal GeTe ($\alpha = 4.2$ eVÅ),[57] the topological insulator Bi_2Se_3 (α can be tuned by field effect up to 1.3 eVÅ),[58] and the Ir(111) surface ($\alpha = 1.3$ eVÅ).[59] Surface alloying and heterostructure design are effective routes to increase the RE even further; e.g., the doped Bi/Ag(111) surface,[60] the 2D dichalcogenides $LaOBiS_2$[61] and $PtSe_2$,[62,63] the heterostructures Tl_2O/PtS_2[64] and $PtSe_2/MoSe_2$[65] are all systems where α is pushed well above 1 eVÅ. In comparison, heterostructures of ordinary semiconductors[66] and oxides[67,68] display α about 2 orders of magnitude smaller, due to the modest SOC amplitude. For what concerns HPs, in the literature, there is a rather large range of estimates for α. From the theoretical side, this is not surprising, insofar as α crucially depends on the static atomic structure considered for the calculation, but for HPs a specific, universally adopted static atomic structure cannot be established. Using molecular dynamics (MD) calculations, on the other hand, it is possible, in principle, to monitor the time evolution of the band structure and the RE splitting, but the results may be largely dependent on the methodology and the parameters used for the simulations (in particular, the supercell size and the simulation time). At the experimental level, several methodologies have been used to reveal

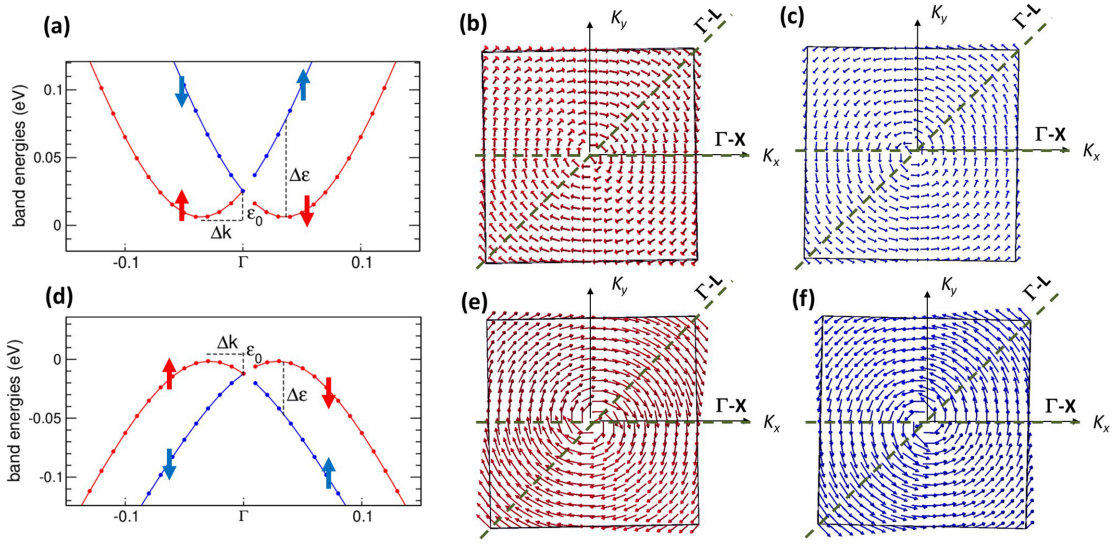

FIG. 1. Calculated band structure for $MAPbI_3$. (a) Conduction bands along the Γ–X direction in the $k_z = 0$ plane of the $\sqrt{2} \times \sqrt{2} \times 2$ tetragonal cell. Values of the Rashba parameters are explained in the text. Red and blue are for clockwise and anticlockwise chiral bands, respectively. (b) and (c) Spin texture in k-space for the band of corresponding color. (d)–(f) are the analogous results for the valence bands. Reprinted with permission from Filippetti *et al.*, J. Phys. Chem. C **123**, 6753–6762 (2019). Copyright 2019 American Chemical Society.

the RE in hybrid perovskites, sometime with contrasting conclusions. In Sec. III, we report an overview of the literature in the field.

III. OVERVIEW OF REPORTED RASHBA EFFECTS IN HYBRID PEROVSKITES

Hybrid perovskites are quite different from ordinary semiconductors characterized by a few, well-defined structural minima, with a static ground state that neatly prevails at any specific temperature. Even at low temperature, in the structurally static phase, the molecular sublattice orientation generates many metastable structural minima, which only differ by a few meV/f.u. from each other and, thus, can be easily swapped by thermal fluctuations. The vast majority of these microstates are electrically polarized[69] and exhibit robust Rashba splitting as a consequence of strong SOC and large dipole fields. In MAPI, dipole fields $\sim 10^7$ V/cm are found at the PbI_2 atomic planes, whose electronic states mostly contribute to the bandgap region.[12] However, in Ref. 69, it is shown that the macroscopic polarization cancels out at high temperature, when averaged over the microstates. The average RE behavior, however, is more complicate to understand. In Ref. 70, it is pointed out that even in a globally centrosymmetric environment, the RE can exist, associated with atomic sites characterized by a polar point group (e.g., in layered antiferroelectric materials). For a 3D macroscopic average of polarized nanodomains with randomly oriented polarization, the RE can be expected to survive only locally, on the nanodomain length scale. Taking the Rashba band splitting in k space $\Delta k \sim 0.02$ Å^{-1}, a crude estimate of the minimal domain length required to appreciate this splitting gives $2\pi/\Delta k \sim 30$ nm. An increasing disorder and temperature will likely reduce this size, causing a progressive suppression of Rashba.

Above the orthorhombic to tetragonal transition temperature, the molecules have enough kinetic energy to rotate with ~ 10 ps frequency, and the structure can only be conceived in dynamical terms. Understanding how this peculiar behavior affects the persistency of RE is a remarkable theoretical challenge. Classical molecular dynamics (MD) simulations[71,72] show that the molecular motion becomes completely decorrelated even on short distances within a few ps, thus ruling out a persistence of polarization on longer timescale. Computationally heavyweight, *ab initio* MD simulations were carried out in Ref. 14 using ~ 3 nm supercells with non-centrosymmetric (*I4cm*) and centrosymmetric (*I4/mcm*) atomic structures for ~ 10 ps simulations; they found sizable RE not only in the *I4cm* ($\alpha \sim 2.8$ eVÅ, and 5 *e*VÅ, for VBT and CBB, respectively) but even in the centrosymmetric *I4/mcm* structure ($\alpha = 1.1$ and 2.2 eVÅ,), as a result of local atomic fluctuations on the nm length scale; these results unveil the intriguing possibility of a dynamical RE persisting up to a few nm length scale. Going beyond this size limit is a prohibitive enterprise for *ab initio* simulations; however, intuition tells us that in globally centrosymmetric systems, the RE is going to be quenched on the macroscopic length scale. Interestingly, the dynamical RE was also found in simulations of inorganic $CsPbI_3$ perovskites, as a consequence of highly anharmonic structural fluctuations.[73] Similar results by *ab initio* MD were obtained in Ref. 74 for MAPbI3 and $CsPbI_3$. However, angle-resolved photoemission (ARPES) experiments on the valence bands of $CsPbI_3$[75] did not confirm this finding. A fiercely contrasting viewpoint is presented in Ref. 76, where second-harmonic generation (SHG) is used to assess the *I4/mcm* as the actual symmetry of tetragonal $MAPbI_3$. This symmetry implies that the RE can be present only at the surface, not in the bulk. Indeed, modeling based on SHG data[77] found very small Rashba values ($\alpha \sim 10^{-3}$ eVÅ). In Ref. 76, calculations are also used to show that, when the PbI_3 atoms of the octahedral cage are kept fixed in centrosymmetric *I4/mcm* positions, the RE generated by pure MA polar alignment is much smaller ($\alpha \sim 0.45$ eVÅ); this is expected, as band extrema are contributed by PbI_3-derived electronic states, and a large portion of the electric polarization in $MAPbI_3$ comes from the PbI_3 distortions.[69] However, we disagree on the fact that by fixing the PbI_3 positions the actual dynamical behavior of the perovskites can be captured, since the inorganic sublattice interacts strongly with the MA orientation. As a matter of fact, both *I4cm* and *I4/mcm* are incompatible with the C_{3v} molecular structure, and thus in our viewpoint, these symmetries lose meaning when interpreted in static terms.

For what concerns the experiments, evidence of RE is no less controversial than for calculations. The most straightforward way to describe the band structure is through angle-resolved photoemission (ARPES), which however is typically limited to the occupied states. Moreover, the RE occurs in a tiny volume (~ 0.1 Å^{-1}) inside the BZ, and thus a remarkably high resolution is required to map the bands with this level of detail. In Ref. 19, ARPES measurements were reported, showing giant Rashba splitting at the valence band top of $MAPbBr_3$, nicely evidenced by a clear-cut, ring torus-shaped Fermi surface; they extracted $\Delta k = 0.043$ Å^{-1}, and $\alpha \sim 7$ eVÅ and 11 eVÅ for orthorhombic and cubic phases, respectively, and huge $\varepsilon_0 = 160$ meV, that is way larger than the $\varepsilon_0 \sim 20$–30 meV values calculated for MAPI. It should be pointed out, however, that ARPES is rather sensitive to the surface, and thus surface polar fields could contribute to amplify these values. A later ARPES experiment for $MAPbBr_3$ valence bands[78] gave a neatly contrasting result: they could not find evidence of such a gigantic Rashba splitting, fixing a limit value $\alpha \sim 1.4$ eVÅ as the maximum compatible with their observations. In all the other ARPES experiments on hybrid perovskites, we are aware that the RE was not reported or not resolved.[79–83] We can also find in the literature a number of experiments that relies on optical measurements. Perhaps the technique most often used to reveal the RE is by photocurrent excitations with circularly polarized light: according to the circular photogalvanic effect (CPE), light helicity can be used to excite a spin-selected photocurrent, thus revealing the different spin orientations associated with two k and $-k$ inter-band transitions connected by the time-reversal symmetry. In Ref. 84, the CPE was observed in $MAPbI_3$ at room temperature and attributed to a dynamical RE. Another approach proposed in Ref. 85 was based on the analysis of the excitonic fine structure splitting in $MAPbI_3$, achieved by coherent quantum beat spectroscopy driven by intense single-cycle terahertz (THz) signal; a modeling was used to assess that that the observed excitonic splitting should be attributed to the dynamical RE. Very recently, a technique based on two-photon absorption spectroscopy was used to reveal the RE in $MAPbI_3$ and $MAPbBr_3$;[86] however, the authors showed that these findings were correlated with the presence of ionic defects and local electric fields.

The experimental evidence becomes stronger and more abundant when moving beyond the horizon of 3D bulk materials. In Ref. 21, the RE was observed in 20-nm $MAPbBr_3$ nanocrystals, revealed by a peak splitting in the transient absorption spectra. This effect, present in both static and dynamic regimes, is attributed to a built-in electric field generated by ultrashort pumping pulse. In Ref. 29, electric

measurements in the magnetic field displayed a magnetoelectric (ME) coupling at the interface between magnetic Co and $MAPbI_{3-x}Cl_x$, whose origin was attributed to the RE; being this ME coupling frequency dependent, this interface is proposed as valuable material for spin-orbitronic applications. In Ref. 23, a robust RE was proved in phenylethylammonium lead iodide perovskite (PEA_2PbI_4), a 2D material with the Ruddlesden–Popper structure. Using a combination of transient spectroscopy, steady-state spectroscopy, and *ab initio* calculations, they measured excitonic and band energy levels, from which a Rashba splitting with $\varepsilon_0 \sim 40$ meV and $\alpha \sim 1.6$ eVÅ was modeled. The RE for the same material was later confirmed by transient absorption spectroscopy,[24] CPE measurements,[27] and two-photon absorption spectroscopy.[86] Also, it was recently reported that circular light photoluminescence is enhanced when doping the 2D perovskite with magnetic Co.[87] Circularly polarized light was also used to investigate 2D Dion–Jacobson lead iodide perovskite,[25] which is structurally similar to PEA_2PbI_4; the Dion–Jacobson compound is found ferroelectric below $T_c = 353$ K, with polarization $P_e \sim 10$ $\mu C/cm^2$; also, a giant room-temperature RE was estimated, with $\varepsilon_0 \sim 85$ meV, $\Delta k \sim 0.067$ Å^{-1}, and $\alpha \sim 2.6$ eVÅ. Rashba splitting was also found in a 2D butylammonium lead iodide.[26,28] Following a different idea, in a recent work,[32] a robust RE with $\varepsilon_0 = 104$ meV and $\alpha \sim 1.62$ eVÅ was revealed in a 3D lead iodide perovskite for a suited mixture of Rb, MA, and FA cations at the A-site, coherently described by *ab initio* calculations and CPE. Finally, in Ref. 30 a variety of $MAPbI_3$ interfaces with graphene and TiO_2 were studied by *ab initio* calculations; depending on the specific terminations, values $\alpha \sim 0.1$–0.6 eVÅ for VBT and $\alpha \sim 0.17$–1.17 eVÅ were obtained.

In summary, this overview suggests that we should distinguish between pristine 3D perovskites and 3D doped or low-dimensional systems, including layered perovskites, surfaces, and interfaces; for the former, it is safe to say that the presence of RE is controversial and cannot be confirmed so far, at least at high temperature. The large variety of sample conditions and measurements, and the objective difficulty in distinguishing between bulk and surface effects explain, at least in part, the lack of a definitive conclusion; methodological improvements and more results will shed new light in the future. On the other hand, there is convincing evidence of robust RE in layered lead iodide perovskites; these are very flexible structural templates which allow a wide spectrum of possibility to modulate and control the Rashba phenomenology by thickness, substrates, and chemical composition, as well as by applied electric, magnetic, radiative, and strain fields. The horizon can be extended to virtually endless combinations including doping and interfaces, which are also reported to be favorable to RE. While still at a preliminary stage, the use of hybrid perovskites for spin-orbitronic technologies appears nowadays as a solid and fascinating perspective.

IV. CHARGE–SPIN CONVERSION IN MAPI

The RE can produce spectacular consequences on the electrodynamic properties of carriers; following again the Zeeman-like modeling of SOC, combining Eqs. (2) and (4), we obtain

$$\begin{aligned} \frac{\partial \varepsilon_{\boldsymbol{\sigma}}}{\partial \sigma_y} &= \mu_B B_{so,y} = \alpha k_x \Rightarrow B_{so,y} = \frac{\alpha}{\mu_B} k_x, \\ \frac{\partial \varepsilon_{\boldsymbol{\sigma}}}{\partial \sigma_x} &= \mu_B B_{so,x} = -\alpha k_y \Rightarrow B_{so,x} = -\frac{\alpha}{\mu_B} k_y. \end{aligned} \tag{10}$$

From Eq. (10), we see that an electron moving along, say x, experiences a spin–orbit magnetic field proportional to the Rashba coefficient, which polarizes the electron spin and generates a spin accumulation and a net magnetization in the y direction perpendicular to the electron current and to the dipole field; analogously, a current along y generates a net magnetization along $-x$. This is the REE illustrated in Fig. 2 for the conduction bands of MAPI.

At room T and below, the electron current is substantially contributed by states at the Fermi energy (ε_F). In Fig. 2, black circles indicate the equilibrium Fermi contour in the (a, b) plane for a reference electron doping $n \sim 10^{19}$ cm^{-3}, corresponding to a Fermi energy $\varepsilon_F = 0.1$ eV. It is easy to realize that the x and y spin components perfectly compensate if integrated around the contour, i.e., no net spin polarization occurs in real space. The situation changes when an external field $\mathcal{E}$ (not to be confused with the internal dipole field $\boldsymbol{E}$) is applied along, e.g., the x axis: the Bloch–Boltzmann theory (BBT)[88,89] shows that in stationary electron current conditions, the Fermi contour shifts by a quantity $\delta k = e\tau\mathcal{E}/\hbar$ in the $-\mathcal{E}$ direction, where τ is the electronic relaxation time. The shifted Fermi circles (drawn in green) display a spin unbalance in the direction y perpendicular to the current: specifically, the bigger Fermi circle on the c band is loaded by a net positive σ_y [Fig. 2(a)], and the smaller Fermi circle on the a band by a net negative σ_y [Fig. 2(b)]; overall, the change in the larger circle prevail, thus generating a net accumulation of the spin in the positive y direction. Analogously, an electric field in the y direction will produce a net spin accumulation σ_x. At very low doping, i.e., when ε_F is lower than ε_0 (below $n \sim 3 \times 10^{18}$ cm^{-3} for bulk MAPI),[12] the spin accumulation is even more significant since a smaller Fermi circle generates a larger fraction of aligned spins (explicit evidence will be given later on). Since the pioneering work of Ganichev *et al.*[90] who demonstrated this effect in n-doped Gas/AlGaAs heterostructures, the REE was then eagerly explored as a mean to switch magnetization in magnetic/non-magnetic heterostructures: the spin accumulation generated by REE diffuses as a spin current and exerts a torque on the magnetization of the ferromagnetic layer (a technique called the spin-transfer torque or spin-torque ferromagnetic resonance).[35,36] The search for ever stronger spin-torque effect pushed the community to explore new materials with very strong SOC, such as the topologically insulating $(BiSb)_2Te_3$[91] and Bi_2Se_3.[92,93] In recent years, a growing experimental evidence has been accumulated on the presence of REE in a number of topological insulator, transition-metal dichalcogenides, and van der Waals heterostructures.[94–99] The inverse Rashba–Edelstein effect (IREE) is also well documented in the literature:[100–103] a spin current is injected into the Rashba material by ferromagnetic resonance across the interface with a magnetic material (spin pumping): an enforced σ_y component causes a shift of the bigger Fermi circle on the c band, thus an electron current in direction $-x$ [Fig. 2(c)], and a shift of the smaller Fermi circle and a corresponding electron current along $+x$ [Fig. 2(d)]; again, the contribution of the bigger Fermi circle prevails, and a net electron current in the $-x$ direction is generated. Finally, it is worth mentioning a quickly evolving measurement technique based on THz photoemission (see Ref. 104 for a recent review): here, femtosecond laser pumping is used to generate a spin current in the ferromagnetic side of the junction; by IREE, this will convert into a transient charge current emitting in the THz range; the THz signal is, thus, signature of the spin–charge conversion. This all-optical technique promises to be a powerful alternative to transport-based

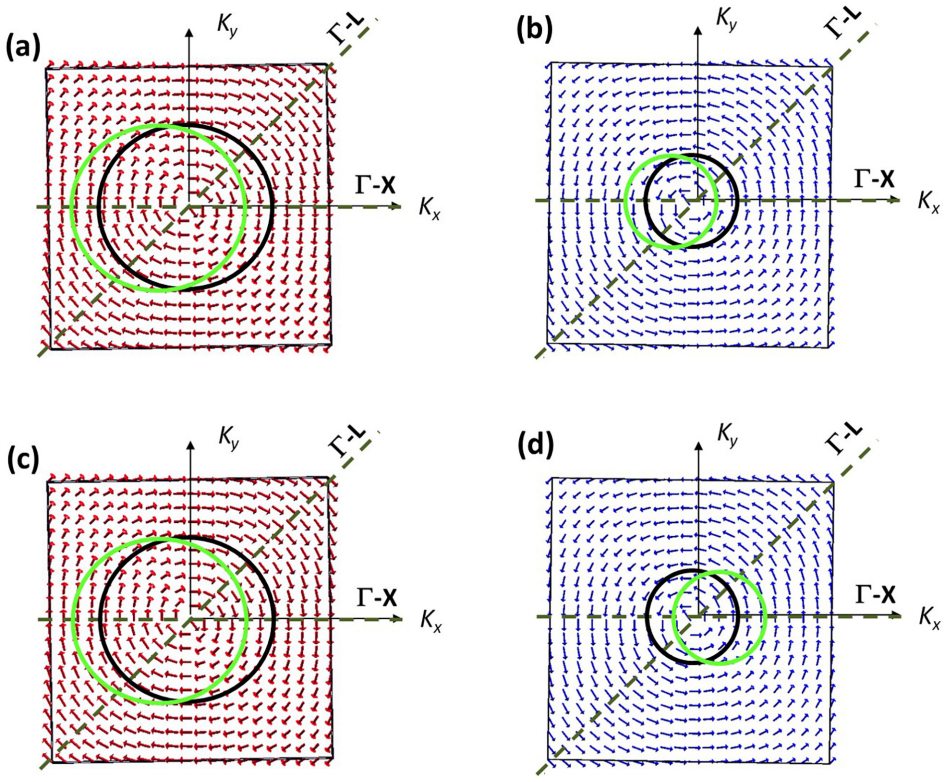

FIG. 2. Spin texture of *c* (red) and *a* (blue) conduction bands calculated for MAPI inside a squared region around Γ of the $k_z = 0$ slice of the BZ (elaborated from Ref. 12). Black and green circles show Fermi contours in equilibrium (black) and under applied field (green). (a) and (b) Shift of the Fermi contours associated with the REE charge–spin conversion. (c) and (d) Analogous shifts associated with the IREE spin–charge conversion (see the text).

measurements to explore REE and IREE, especially for those Rashba semiconductors, such as HPs, which can be hardly doped by chemical means.

V. BLOCH–BOLTZMANN MODEL OF REE IN PEROVSKITES

A quantitative evaluation of the current-induced spin accumulation in perovskites can be performed using the BBT fed by calculated band structure. However, the accurate numerical integration in a tiny region of the BZ can be computationally cumbersome. In the following, we will consider instead a more agile analytic approach based on the RE model of Eqs. (6)–(8). As a further simplification, we develop the formulation in 2D, which is probably the most technologically relevant case. Our approach is similar to that previously introduced by Silsbee,[105,106] which, however, was appropriate for the high charge density limit, i.e., Δk much smaller than the Fermi vector. Here, we develop a formulation valid at any charge concentration, thus even in the limit of very low charge density, that is the case where charge–spin conversion is more effective. We start from the high-doping regime, where both *c* and *a* bands are populated. The Boltzmann distribution function $f(\mathbf{k})$ can be approximated, to the linear order in $\mathcal{E}$, as the Fermi–Dirac function $f_0(\mathbf{k} - \delta\mathbf{k})$ calculated for a crystalline momentum back-shifted by a quantity (suppose $\mathcal{E}$ applied along positive *x*) $\delta k_x = -e\tau\mathcal{E}/\hbar$; thus,

$$f_0(\mathbf{k} - \delta\mathbf{k}) \sim f_0(\mathbf{k}) + \frac{e\tau}{\hbar}\frac{\partial f_0}{\partial k_x}\mathcal{E} = f_0(\mathbf{k}) + \frac{e\tau}{\hbar}\frac{\partial f_0}{\partial \varepsilon}\frac{\partial \varepsilon}{\partial k_x}\mathcal{E}. \tag{11}$$

From the BZ average of the band velocity, we obtain the drift velocity (not including factor 2 due to spin degeneracy)

$$\langle v_x \rangle_{c,a} = \frac{e\mathcal{E}}{n_{c,a}} \int d\mathbf{k}\, g(\mathbf{k})\tau(\mathbf{k})\, \frac{\partial f_0}{\partial \varepsilon_{c,a}} v^2_{x,(c,a)}(\mathbf{k}), \tag{12}$$

where $n_{c,a}$ and $v_{x,(c,a)}$ are charge density and band velocity associated with *c* and *a* bands, respectively, and $g(\mathbf{k}) = 1/(2\pi)^2$. From $\langle v_x \rangle = -\mu_x \mathcal{E}$, we can extract the 2D electron mobility

$$\mu_{x(c,a)} = -\frac{e}{4\pi^2 n_{c,a}} \int d\mathbf{k}\, \tau(\mathbf{k})\, \frac{\partial f_0}{\partial \varepsilon_{c,a}} v^2_{x,(c,a)}(\mathbf{k}). \tag{13}$$

In 2D, $k_p = k$ and we can use radial coordinates; also, it is a reasonable approximation taking τ as energy-dependent and fixing it to the ε_F value; so, we can rewrite

$$\mu_{x(c,a)} = -\frac{e\,\tau}{4\pi^2 n_{c,a}} 2\pi \int dk\, k\, \frac{\partial f_0}{\partial \varepsilon_{c,a}} v^2_{x,(c,a)}(\mathbf{k}), \tag{14}$$

where 2π comes from the angle integration, being the integrand not angle-dependent. At room T, the f_0 derivative can be conveniently approximated as a delta function centered at ε_F

$$\frac{\partial f_0}{\partial \varepsilon_{c,a}} \sim -\delta(\varepsilon_{c,a} - \varepsilon_F) = -\frac{\delta(k - k_{Fc,a})}{|\nabla_k \varepsilon_{c,a}|_{k_{Fc,a}}}. \tag{15}$$

Thus, the integral in *k* reduces to the integrand calculated at the Fermi radius of the two bands; we can conveniently redefine

$k_{Fc,a} = k_F \pm \Delta k$, where k_F is the Fermi vector of the 2D Fermi gas with equivalent ε_F [see Fig. 3(a)]. From Eq. (6), we have

$$\left.\frac{\partial \varepsilon_{c,a}}{\partial k}\right|_{k_{Fc,a}} = \frac{\hbar^2 k_{Fc,a}}{m^*} \mp \alpha = \frac{\hbar^2 k_F}{m^*}. \tag{16}$$

Also, assuming a planarly homogeneous system, we can replace the squared Fermi velocity with its planar average $(v_x^2 + v_y^2)/2$; through elemental manipulation, we obtain

$$\begin{aligned}\frac{v_{x,(c,a)}^2 + v_{y,(c,a)}^2}{2} &= \frac{\hbar^2 k_{Fc,a}^2}{2m^{*2}} \mp \frac{\alpha}{m^*} k_{Fc,a} + \frac{\alpha^2}{2\hbar^2} \\ &= \frac{\hbar^2}{2m^{*2}} (k_{Fc,a} \mp \Delta k)^2 = \frac{\hbar^2 k_F^2}{2m^{*2}}.\end{aligned} \tag{17}$$

Here, we can note that the planar velocity on the Fermi circle is independent of the SOC deformation. Inserting results of Eqs. (13)–(15) in Eq. (12), we have

$$\mu_{x(c,a)} = \frac{e\,\tau}{2\,\pi\, n_{c,a}} \int dk\, k\, \frac{\delta(k - k_{Fc,a})}{\frac{\hbar^2 k_F}{m^*}} \frac{\hbar^2 k_F^2}{2m^{*2}} = \frac{e\,\tau k_F (k_F \pm \Delta k)}{4\,\pi\, n_{c,a} m^*}. \tag{18}$$

The value of k_F must be determined from the total carrier density included in the Rashba bands. We have [see Fig. 3(a)]

$$n_{c,a} = \frac{1}{4\pi^2} \int_0^{k_{Fc,a}} d^2k = \frac{k_{Fc,a}^2}{4\pi} = \frac{(k_F \pm \Delta k)^2}{4\pi}, \tag{19}$$

$$n = n_c + n_a = \frac{(k_F^2 + \Delta k^2)}{2\pi}; \quad k_F = \sqrt{2\pi n - \Delta k^2}, \tag{20}$$

from which we extract k_F and, in turn, $n_{c,a}$. From Eq. (20), we obtain

$$\mu_{x(c,a)} = \frac{e\,\tau}{m^*} \frac{k_F}{(k_F \pm \Delta k)}. \tag{21}$$

We notice the explicit dependence of the mobility on n (through k_F) which marks a radical departure from the Drude-like behavior. Specifically, the mobility of the Dirac-cone shaped a band is larger than its Drude counterpart, while the c band mobility is smaller. We emphasize that this behavior is not a material feature, but a direct consequence of the peculiar band topology induced by the RE. The resulting average mobility is

$$\mu_x = \frac{n_c \mu_{x,c} + n_a \mu_{x,a}}{n} = \frac{e\,\tau}{m^*} \frac{1}{1 + \left(\frac{\Delta k}{k_F}\right)^2}. \tag{22}$$

Thus, the k_F dependence is not canceled out in the average. The Drude result is recovered only in the high-density limit $\Delta k/k_F \sim 0$, i.e., when c and a coalesce to the same parabolic band; this is expected since in the low-T limit and for parabolic band approximation, the BBT must converge to the Drude theory. In the same limit, we see from Eq. (18) that n recovers the 2D Fermi gas result. The current density associated with the two bands is

$$J_{x(c,a)} = -e\, n_{c,a} \mu_{x(c,a)} \mathcal{E} = -\frac{e^2 \mathcal{E}\,\tau}{4\pi m^*} k_F (k_F \pm \Delta k). \tag{23}$$

The total current density is

$$J_x = J_{x,c} + J_{x,a} = -\frac{e^2 \mathcal{E}\,\tau}{2\pi m^*} k_F^2. \tag{24}$$

For the calculation of the spin density in 2D, we follow an analogous development; using again radial coordinates, the BZ-averaged spin vector is

$$\begin{aligned}\langle \boldsymbol{\sigma}_{c,a} \rangle &= \frac{e\,\tau \mathcal{E}}{4\,\pi^2 n_{c,a}} \int d\mathbf{k}\, \frac{1}{k} \begin{pmatrix} \pm k_y \\ \mp k_x \end{pmatrix} \frac{\partial f_0}{\partial \varepsilon_{c,a}} v_{x,(c,a)}(\mathbf{k}) \\ &= \frac{e\,\tau \mathcal{E}}{4\,\pi^2 n_{c,a}} \int d\phi \cos\phi \int dk \begin{pmatrix} \pm k \sin\phi \\ \mp k \cos\phi \end{pmatrix} \frac{\partial f_0}{\partial \varepsilon_{c,a}} v_{x,(c,a)}(\mathbf{k}).\end{aligned} \tag{25}$$

The band velocity is

$$v_{x,(c,a)} = \frac{\hbar k_x}{m^*} \mp \frac{\alpha}{\hbar} \frac{k_x}{k} = \frac{\hbar k \cos\phi}{m^*} \mp \frac{\alpha}{\hbar} \cos\phi = \frac{\hbar}{m^*} \cos\phi (k \mp \Delta k). \tag{26}$$

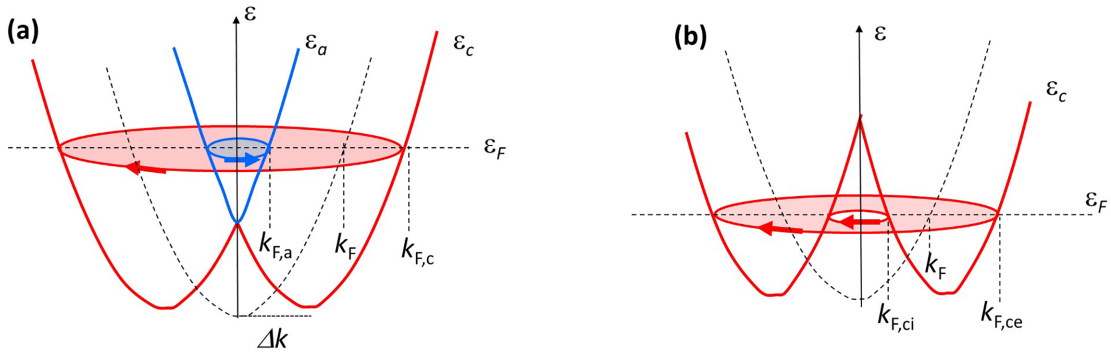

FIG. 3. Sketch of the conduction bands according to the RE model. (a) High-density regime; red and blue curves draw c and a band energies, respectively; $k_{F,c}$ and $k_{F,a}$ are the corresponding Fermi vectors; arrows indicate their opposite spin chirality. The spin-degenerate paraboloid (dashed black line) with bottom aligned to the CBB represents the 2D Fermi gas of equivalent Fermi energy, and k_F its corresponding Fermi vector. In this regime, $\varepsilon_F > \varepsilon_0$, $k_F > \Delta k$; red and blue shaded areas are the 2D Fermi areas of the two bands, from which k_F is determined. (b) Low-density regime; now only the c band is occupied; the 2D Fermi surface is composed of two circles associated with the internal (ci) and external (ce) band portion, with $k_{F,ci}$ and $k_{F,ce}$ Fermi vectors and same spin chirality. Here, $\varepsilon_F < \varepsilon_0$, $k_F < \Delta k$. The red shaded disk is the 2D Fermi area from which k_F is determined.

Using the results of Eqs. (13) and (14), we have

$$\langle \boldsymbol{\sigma}_{c,a} \rangle = -\frac{e\tau\mathcal{E}}{4\pi^2 n_{c,a} \hbar k_F} \int d\phi \cos\phi \int dk \begin{pmatrix} \pm k \sin\phi \\ \mp k \cos\phi \end{pmatrix} \delta(k - k_{Fc,a})(k \mp \Delta k)$$
$$= -\frac{e\tau\mathcal{E}}{4\pi^2 n_{c,a} \hbar k_F} k_{Fc,a}(k_{Fc,a} \mp \Delta k) \int d\phi \cos\phi \begin{pmatrix} \pm \sin\phi \\ \mp \cos\phi \end{pmatrix}. \quad (27)$$

From

$$\int_0^{2\pi} d\phi \begin{pmatrix} \pm \sin\phi \\ \mp \cos\phi \end{pmatrix} \cos\phi = \begin{pmatrix} 0 \\ \mp\pi \end{pmatrix}, \quad (28)$$

we obtain the expected result that only the σ_y component is non vanishing; from $k_{Fc,a} = k_F \pm \Delta k$, we finally have (since now on it is understood that this is the y spin component)

$$\langle \sigma_{c,a} \rangle = \pm \frac{e\tau\mathcal{E}}{4\pi n_{c,a}\hbar} k_{Fc,a} = \pm \frac{e\tau\mathcal{E}}{4\pi n_{c,a}\hbar}(k_F \pm \Delta k). \quad (29)$$

So, c and a bands have positive and negative spin components along y, but the former prevails due to the larger Fermi radius. The value in Eq. (25) is the adimensional spin-polarization fraction per electron in 2D; multiplying by the electron density, we obtain the 2D spin density of the two bands:

$$n^s_{c,a} = n_{c,a}\langle \sigma_{c,a} \rangle = \pm \frac{e\tau\mathcal{E}}{4\pi\hbar}(k_F \pm \Delta k). \quad (30)$$

The net spin density is

$$n^s = n_c\langle \sigma_c \rangle + n_a \langle \sigma_a \rangle = \frac{e\tau\mathcal{E}}{2\pi\hbar}\Delta k = \frac{\delta k \Delta k}{2\pi}. \quad (31)$$

So, the spin density is proportional to Δk (i.e., to m^* and α) and to the Fermi circle shift amplitude δk generated by the applied field. The net spin polarization fraction,

$$\langle \sigma \rangle = \frac{n^s}{n} = \frac{e\tau\mathcal{E}}{2\pi\hbar n}\Delta k = \frac{\delta k \Delta k}{k_F^2 + \Delta k^2}, \quad (32)$$

grows inversely to the squared Fermi vector; thus, for a given applied field, the spin polarization is larger at lower carrier concentration; in fact, from Fig. 2, it is easy to realize that as the Fermi circle becomes smaller, the fraction of aligned spins along the Fermi circle increases. On the other hand, the spin density $n^s = n\langle \sigma \rangle$ is independent of k_F, and its only dependence on the charge density occurs through the relaxation time present in δk. Ultimately, the spin–charge coupling can be quantified by the ratio

$$\frac{n^s}{j} = \frac{m^*}{e\hbar}\frac{\Delta k}{k_F^2}, \quad (33)$$

which in 2D has $(\text{A m})^{-1}$ dimension; this is maximized by a large effective mass, a large Rashba splitting Δk, and a small carrier concentration. In terms of spin polarization to current ratio

$$\frac{\langle \sigma \rangle}{j} = \frac{n^s}{nj} = \frac{2\pi m^*}{e\hbar}\frac{\Delta k}{k_F^2(k_F^2 + \Delta k^2)}. \quad (34)$$

In the low-density regime ($\varepsilon_F < \varepsilon_0$, $k_F < \Delta k$), two Fermi circles are populated, both on the c band, labeled ce and ci [see Fig. 3(b)], whose corresponding Fermi vectors are $k_{Fce,ci} = \Delta k \pm k_F$. Substituting these values in Eq. (16), we obtain for the mobility on ce and ci circles

$$\mu_{ce,ci} = \frac{e\tau k_F(\Delta k \pm k_F)}{4\pi n_{ce,ci} m^*}. \quad (35)$$

Now k_F must be recalculated for the low-density regime. The 2D Fermi area is the disk enclosed between outer and inner circles [Fig. 3(b)], thus

$$n = n_{ce} - n_{ci} = \frac{1}{4\pi}\left[(\Delta k + k_F)^2 - (\Delta k - k_F)^2\right] = \frac{\Delta k\, k_F}{\pi}. \quad (36)$$

Clearly, Eqs. (36) and (20) give the same $n = \Delta k^2/\pi$ at the critical point $\Delta k = k_F$ connecting the two regimes; as expected, a bigger Rashba coefficient expands the n range of the low-density regime. The averaged mobility is then

$$\mu = \frac{n_{ce}\mu_{ce} + n_{ci}\mu_{ci}}{n} = \frac{e\tau k_F \Delta k}{2\pi n m^*} = \frac{e\tau}{2m^*}. \quad (37)$$

Again, Eqs. (37) and (21) coincide for $\Delta k = k_F$. For the current density, adding ce and ci contributions we recover the same expression obtained at high-density in Eq. (21). For the spin polarization fraction, we obtain

$$\langle \sigma_{ce,ci} \rangle = \frac{e\tau\mathcal{E}}{4\pi n_{ce,ci}\hbar} k_{Fce,ci} = \frac{e\tau\mathcal{E}}{4\pi n_{ce,ci}\hbar}(\Delta k \pm k_F). \quad (38)$$

Thus, both circles give a positive contribution to the magnetization along y; for the total spin density,

$$n^s = n_{ce}\langle \sigma_{ce} \rangle + n_{ci}\langle \sigma_{ci} \rangle = \frac{e\tau\mathcal{E}}{2\pi\hbar}\Delta k = \frac{\delta k \Delta k}{2\pi}, \quad (39)$$

which is the same expression obtained for high density in Eq. (30); for the spin polarization fraction,

$$\langle \sigma \rangle = \frac{n^s}{n} = \frac{\delta k}{2\pi n}\Delta k = \frac{\delta k}{2k_F}. \quad (40)$$

So, the spin polarization is proportional to the Rashba coefficient and inversely proportional to n. Finally, at low-density,

$$\frac{\langle \sigma \rangle}{j} = \frac{\pi m^*}{e\hbar}\frac{1}{k_F^3} = \frac{m^*}{e\pi^2\hbar n^3}\Delta k^3. \quad (41)$$

From Eq. (41), it is clear that the efficiency of the charge–spin conversion mechanism decreases very rapidly with the decrease in the Rashba coefficient and the increase in the charge density. As significant example, in Fig. 4, we report numerical results obtained for a hypothetical 2D slab of MAPI at room T; we establish a relation $n_{3D} = n_{2D}/t$ between 3D and 2D densities by fixing a slab thickness $t = N_l c \sim 10$ nm, where $N_l = 8$ is the number of layers and $c = 12.67$ Å the cell length in the orthogonal direction. For a qualitative analysis, we assumed typical bulk values for the Rashba coefficient ($\alpha = 1.2$ eVÅ^{-1}) and for the mass ($m^* = 0.2$). The relaxation time is evaluated using a well-tested analytical approach, including impurity and electron–phonon scattering, previously applied to bulk $MAPbI_3$.[107] This approach describes the scattering with the energy-lowest polar optical phonon as the dominant at room T, in agreement with other reports,[108–111] and accounts for mobility values $\mu \sim 40$–50 cm^2/Vs typically measured in

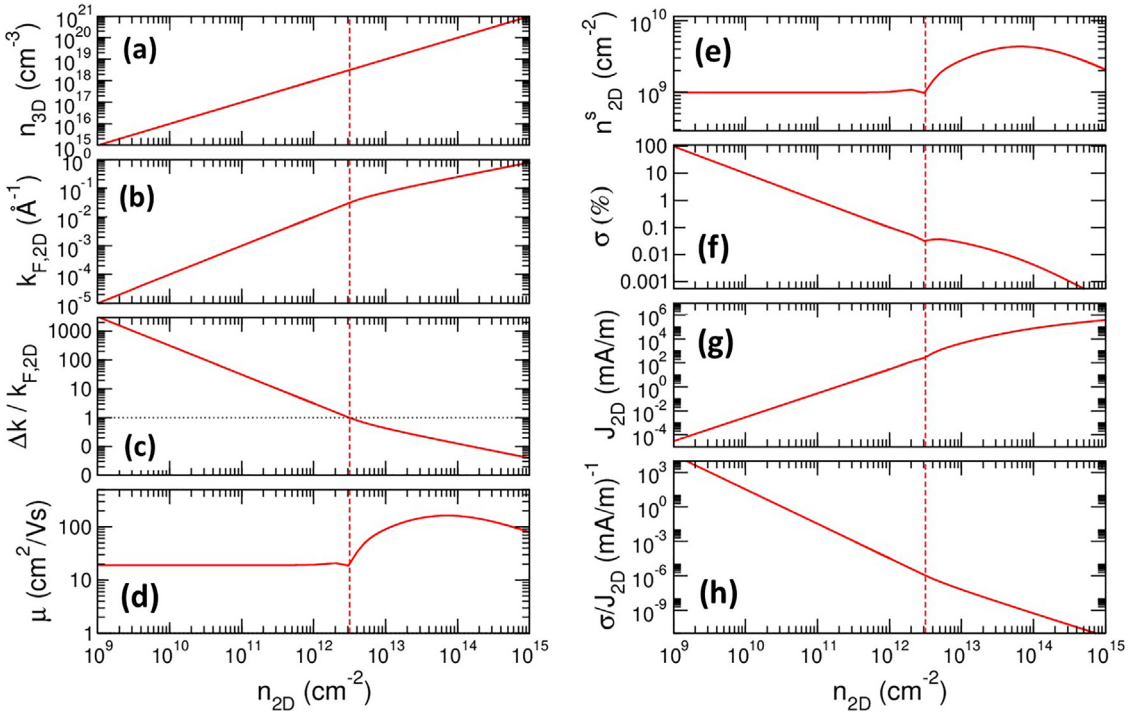

FIG. 4. Results for the 2D Rashba model at room temperature for a 10 nm slab of MAPI. (a) 3D equivalent charge density. (b) Fermi vector. (c) *k*-space splitting to Fermi vector ratio; this is the order parameter for the transition between low-density and high-density regime, evidenced by the dotted line. (d) Electron mobility; (e): spin-density. (f) Spin-polarization fraction. (g) Current density. (h) Spin to current density ratio.

experiments.[112,113] All quantities in Fig. 4 are reported as a function of n_{2D} in an interval range coherent with the carrier concentrations typically explored in optoelectronic experiments. Overall, a net regime change is visible at the critical density $n_{2D} = 3.17 \times 10^{12}\,\mathrm{cm}^{-2}$ (highlighted by the dashed vertical lines in the figure) corresponding to $n_{3D} = 3.12 \times 10^{18}\,\mathrm{cm}^{-3}$. This behavior can be traced back to the Fermi vector [Fig. 4(b)], whose linear growth changes slope at the critical point $k_F = \Delta k$; in fact, this is where the *a* band starts to fill, generating a jump in the density of states and slowing down the growth of k_F vs n_{2D}.

We can also see a dramatic change of mobility [Fig. 4(c)] while moving from the low-density, Drude-like behavior, to the high-density regime, to whom even the *a* band contributes with its high, Dirac cone-derived mobility. A closer look around the critical point reveals a sudden downturn, followed by a region of fast increase. The kink occurs at a Fermi energy ~ 10 meV corresponding to the lowest polar optical phonon $\hbar\omega_{LO}$;[114] indeed, for $\varepsilon_F < \hbar\omega_{LO}$, the phonon can only be absorbed, while for $\varepsilon_F > \hbar\omega_{LO}$, it can be both absorbed and emitted; it follows that the scattering probability first increases at $\varepsilon_F = \hbar\omega_{LO}$, then quickly decreases as ε_F becomes greater than $\hbar\omega_{LO}$. In Fig. 4(e), the spin density generated by an external field $E = 300$ V/cm is shown. Surprisingly, n^s reflects very closely the mobility through all the examined charge density range, despite being not explicitly dependent on *n*. In fact, it is the indirect dependence through the relaxation time, in turn related to ε_F and k_F, which primarily rules the n^s behavior. In the constant regime, for the considered applied field we obtain $n^s_{2D} \sim 10^9\,\mathrm{cm}^{-2}$, corresponding to a spin polarization fraction [Fig. 4(f)] $\sigma \sim 10\%$–100% in the doping range $n_{2D} = 10^9$–$10^{10}\,\mathrm{cm}^{-2}$ (i.e., $n_{3D} = 10^{15}$–$10^{16}\,\mathrm{cm}^{-3}$), and $\sigma \sim 1\%$ for $n_{2D} = 10^{11}\,\mathrm{cm}^{-2}$ ($n_{3D} = 10^{17}\,\mathrm{cm}^{-3}$). For larger charge densities, σ quickly disappears, and thus the charge–spin conversion seems too small to be useful for practical purposes. Of course, larger σ values can be obtained using stronger external fields, but this would not be reflected in the conversion efficiency proportional to the σ/J_{2D} ratio [Fig. 4(h)], which is unaffected by $\mathcal{E}$. Thus, according to our analysis, a significant implementation of the REE in HPs requires the accurate manipulation of 2D charge densities lower than $10^{11}\,\mathrm{cm}^{-2}$. The conversion efficiency can be increased, at the intrinsic level, by a larger Rashba coefficient and/or larger effective masses. As for the slab thickness, in our simple design, it does not affect the final results since we assume the Rashba coupling uniform through the slab layers; in actual simulations, however, the band structure would be deeply affected by the distance from the surface, and thus the thickness of the slab could become a crucial ingredient.

Finally, we remark that a direct comparison of our results with the experiments is difficult since what is typically measured in output of charge–spin conversion is the spin current that propagates across the interface between the Rashba material and a magnetic metal layer.[115] Spin current and spin density are related through a continuity equation[116–118] whose theoretical solution is outside our present theoretical framework, and additional work will be required to extend the model to fully realistic device simulation.

VI. CONCLUDING REMARKS

In this work, the perspectives of HPs as materials for spin-orbitronic applications have been examined on the basis of the

abundant literature produced in the last few years, reporting theoretical and experimental results on the spin–orbit properties of a large variety of lead-halide based compounds. Some peculiar features of the HPs optimally fit with the fundamental requirements for the design of SOC-based applications: the bandgap region derived from high-mobility extended states with strong SOC, associated with the molecular sublattice easily orientable to furnish a built-in polarization axis, conjure the ideal situation for a strong, electrically or optically switchable RE. Furthermore, experiments show that circularly polarized light can be used to optically induce spin-polarized carriers with spin coherence lifetime of *ps* order. On the other hand, factors working against this ideal picture are the fast molecular rotations that characterize the room-T phase of 3D HPs and the possible presence of bound excitons and/or disorder-induced charge localization, which disrupt the charge mobility of the injected carriers. While the analysis of the literature does not lend itself to a unique and straightforward conclusion, a distinction emerges between pristine 3D bulk perovskites, and low-dimensional materials including surfaces, interfaces, and thin films, or even 3D doped perovskites. For the latter, the experimental evidence of RE related phenomena is abundant and consistently reported in a variety of different systems. Thus, while we do not rule out the possibility to stabilize robust RE in 3D materials, the 2D environment appears as the most promising for the implementation of SOC-based device technology. For a qualitative evaluation of the charge–spin conversion mechanism in 2D HPs, we have developed a theoretical approach based on Rashba band modeling and the Bloch–Boltzmann theory of the electron transport. Albeit at an ideal level, the model describes a number of fascinating aspects related to the topological nature of the Rashba bands; especially interesting is the transition from the low charge to the high charge regime, accompanied by a non-Drude behavior and a corresponding jump in the mobility above the transition point, caused by the occupancy of the Dirac cone. This rise of mobility is also reflected in the spin density, which in our model is proportional to the electronic relaxation time. From the applicative viewpoint, we found the low-density region to be, by far and large, the most important for what concern the REE efficiency; in fact, spin polarization $\sim 1\%$ or larger requires 2D charge densities $\sim 10^{11}\,\mathrm{cm}^{-2}$ or lower, corresponding to a 3D charge density $\sim 10^{17}\,\mathrm{cm}^{-3}$ for a MAPI slab of 10 nm thickness. For larger charge densities, the conversion efficiency quickly vanishes, since the spin to current ratio is found to decrease as the third power of the Fermi vector. Thus, the capability to accurately manipulate small amount of charges by electrical or optical means seems to be essential in order to distinctly observe the charge–spin conversion. Also, the spin–current ratio depends on the third power of the Rashba k-space shift $\Delta k = \alpha m^*/\hbar^2$, and thus a large Rashba coefficient and effective mass both benefit a robust REE. Finally, we emphasize that these general guidelines should be taken as indicative and tested against the results obtained from realistic band structures. In particular, 2D materials may present peculiar features, such as localized surface or interface states, as well as bound excitons, which could deeply affect the bandgap region and dramatically alter the RE phenomenology.

ACKNOWLEDGMENTS

A.F. and P.W. acknowledge financial support from PRIN2017 Project "TOPSPIN," funded by the Italian Ministry of University and Research. A.M. acknowledges CNR for funding under Project Nos. CNR-RFBR B55F21000620005 and STM2020 56275/2020, and CINECA for awarding access to high-performance computing resources under No. ISCRA IsC96_FFBeNCT.

AUTHOR DECLARATIONS

Conflict of Interest

The authors have no conflicts to disclose.

Author Contributions

Alessio Filippetti: Conceptualization (lead); Data curation (lead); Methodology (lead); Software (lead); Supervision (lead); Writing – original draft (lead). **Payal Wadhwa:** Conceptualization (supporting); Methodology (supporting); Software (supporting); Writing – original draft (supporting); Writing – review & editing (supporting). **Claudia Caddeo:** Conceptualization (supporting); Methodology (supporting); Software (supporting); Writing – original draft (supporting); Writing – review & editing (supporting). **Alessandro Mattoni:** Conceptualization (supporting); Methodology (supporting); Writing – original draft (supporting); Writing – review & editing (supporting).

DATA AVAILABILITY

The data that support the findings of this study are available from the corresponding author upon reasonable request.

REFERENCES

[1]E. I. Rashba, Phys. Solid State **2**, 1224–1238 (1960).
[2]Y. A. Bychkov and E. I. Rashba, JETP Lett. **39**, 78–81 (1984).
[3]Y. A. Bychkov and E. I. Rashba, J. Phys. C **17**, 6039–6045 (1984).
[4]M. Kim, J. Im, A. J. Freeman, J. Ihm, and H. Jin, Proc. Natl. Acad. Sci. U. S. A. **111**, 6900 (2014).
[5]M. Kepenekian, R. Robles, C. Katan, D. Sapori, L. Pedesseau, and J. Even, ACS Nano **9**, 11557–11567 (2015).
[6]F. Zheng, L.-Z. Tan, S. Liu, and A. M. Rappe, Nano Lett. **15**, 7794 (2015).
[7]L. Leppert, S. E. Reyes-Lillo, and J. B. Neaton, J. Phys. Chem. Lett. **7**, 3683–3689 (2016).
[8]S. Hu, H. Gao, Y. Qi, Y. Tao, Y. Li, J. R. Reimers, M. Bokdam, C. Franchini, D. Di Sante, A. Stroppa, and W. Ren, J. Phys. Chem. C **121**, 23045–23054 (2017).
[9]Z.-G. Yu, Phys. Chem. Chem. Phys. **19**, 14907 (2017).
[10]X. Zhang, J.-X. Shen, W. Wang, and C. G. Van de Walle, ACS Energy Lett. **3**(10), 2329–2334 (2018).
[11]X. Zhang, J.-X. Shen, and C. G. Van de Walle, J. Phys. Chem. Lett. **9**(11), 2903–2908 (2018).
[12]A. Filippetti, C. Caddeo, A. Bosin, P. Delugas, and A. Mattoni, J. Phys. Chem. C **123**, 6753−−6762 (2019).
[13]P. Azarhoosh, S. McKechnie, J. M. Frost, A. Walsh, and M. van Schilfgaarde, APL Mater. **4**, 091501 (2016).
[14]T. Etienne, E. Mosconi, and F. De Angelis, J. Phys. Chem. Lett. **7**, 1638–1645 (2016).
[15]E. M. Hutter, M. C. Gélvez-Rueda, A. Osherov, V. Bulovic, F. C. Grozema, S. D. Stranks, and T. J. Savenije, Nat. Mater. **16**, 115–120 (2017).
[16]T. Wang, B. Daiber, J. M. Frost, S. A. Mann, E. C. Garnett, A. Walsh, and B. Ehrler, Energy Environ. Sci. **10**, 509–515 (2017).
[17]V. Sarritzu, N. Sestu, D. Marongiu, X. Chang, Q. Wang, S. Masi, S. Colella, A. Rizzo, A. Gocalinska, E. Pelucchi, M. L. Mercuri, F. Quochi, M. Saba, A. Mura, and G. Bongiovanni, Adv. Opt. Mater. **6**, 1701254 (2018).
[18]J. M. Richter, K. Chen, A. Sadhanala, J. Butkus, J. P. H. Rivett, R. H. Friend, B. Monserrat, J. M. Hodgkiss, and F. Deschler, Adv. Mater. **30**, 1803379 (2018).

[19]D. Niesner, M. Wilhelm, I. Levchuk, A. Osvet, S. Shrestha, M. Batentschuk, C. Brabec, and T. Fauster, Phys. Rev. Lett. **117**, 126401 (2016).
[20]A. G. Lehmann, F. Congiu, D. Marongiu, A. Mura, A. Filippetti, A. Mattoni, M. Saba, G. Pegna, V. Sarritzu, F. Quochi, and G. Bongiovanni, Phys. Chem. Chem. Phys. **23**, 3233–3245 (2021).
[21]Y. D. Glinka, R. Cai, J. Li, T. He, and X. W. Sun, AIP Adv. **10**, 105034 (2020).
[22]M. Isarov, L. Z. Tan, M. I. Bodnarchuk, M. V. Kovalenko, A. M. Rappe, and E. Lifshitz, Nano Lett. **17**, 5020–5026 (2017).
[23]Y. Zhai, S. Baniya, C. Zhang, J. Li, P. Haney, C.-X. Sheng, E. Ehrenfreund, and Z. V. Vardeny, Sci. Adv. **3**, e1700704 (2017).
[24]J. Yin, P. Maity, L. Xu, A. M. El-Zohry, H. Li, O. M. Bakr, J.-L. Brédas, and O. F. Mohammed, Chem. Mater. **30**, 8538 (2018).
[25]I.-H. Park, Q. Zhang, K. C. Kwon, Z. Zhu, W. Yu, K. Leng, D. Giovanni, H. S. Choi, I. Abdelwahab, Q.-H. Xu, T. C. Sum, and K. P. Loh, J. Am. Chem. Soc. **141**, 15972–15976 (2019).
[26]S. B. Todd, D. B. Riley, A. Binai-Motlagh, C. Clegg, A. Ramachandran, S. A. March, J. M. Hoffman, I. G. Hill, C. C. Stoumpos, M. G. Kanatzidis, Z.-G. Yu, and K. C. Hall, APL Mater. **7**, 081116 (2019).
[27]X. Liu, A. Chanana, U. Huynh, F. Xue, P. Haney, S. Blair, X. Jiang, and Z. V. Vardeny, Nat. Commun. **11**, 323 (2020).
[28]M. T. Pham, E. Amerling, H. M. Luong, H. T. Pham, G. K. Larsen, L. Whittaker-Brooks, and T. D. Nguyen, Sci. Rep. **10**, 4964 (2020).
[29]M. Li, L. Li, R. Mukherjee, K. Wang, Q. Liu, Q. Zou, H. Xu, J. Tisdale, Z. Gai, I. N. Ivanov, D. Mandrus, and B. Hu, Adv. Mater. **29**, 1603667 (2017).
[30]C. W. Myung, S. Javaid, K. S. Kim, and G. Lee, ACS Energy Lett. **3**, 1294 (2018).
[31]H. Xu, P. Prabhakaran, S. Choi, M. Wang, K.-S. Lee, and B. Hu, J. Phys. Chem. Lett. **11**, 1–6 (2020).
[32]A. Yusoff, A. Mahata, M. Vasilopoulou, H. Ullah, B. Hu, W. J. da Silva, F. K. Schneider, P. Gao, A. V. Ievlev, Y. Liu, O. S. Ovchinnikova, F. De Angelis, and M. K. Nazeeruddin, Mater. Today **46**, 18–27 (2021).
[33]B. Cai, X. Chen, M. Xie, S. Zhang, X. Liu, J. Yang, W. Zhou, S. Guoa, and H. Zeng, Mater. Horiz. **5**, 961 (2018).
[34]W. Ning, J. Bao, Y. Puttisong, F. Moro, L. Kobera, S. Shimono, L. Wang, F. Ji, M. Cuartero, S. Kawaguchi, S. Abbrent, H. Ishibashi, R. De Marco, I. A. Bouianova, G. A. Crespo, Y. Kubota, J. Brus, D. Y. Chung, L. Sun, W. M. Chen, M. G. Kanatzidis, and F. Gao, Sci. Adv. **6**, eabb5381 (2020).
[35]I. M. Miron, G. Gaudin, S. Auffret, B. Rodmacq, A. Schuhl, S. Pizzini, J. Vogel, and P. Gambardella, Nat. Mater. **9**, 230–234 (2010).
[36]I. M. Miron, K. Garello, G. Gaudin, P.-J. Zermatten, M. V. Costache, S. Auffret, S. Bandiera, B. Rodmacq, A. Schuhl, and P. Gambardella, Nature **476**, 189–194 (2011).
[37]L. Liu, C.-F. Pai, Y. Li, H. W. Tseng, D. C. Ralph, and R. A. Buhrman, Science **336**, 555 (2012).
[38]A. Manchon, H. C. Koo, J. Nitta, S. M. Frolov, and R. A. Duine, Nat. Mater. **14**, 871–882 (2015).
[39]W. Han, Y. Otani, and S. Maekawa, npj Quant. Mater. **3**, 27 (2018).
[40]S. Datta, Nat. Electron. **1**, 604 (2018).
[41]R. M. Lutchyn, T. D. Stanescu, and S. D. Sarma, Phys. Rev. Lett. **106**, 127001 (2011).
[42]C. H. L. Quay, T. L. Hughes, J. A. Sulpizio, L. N. Pfeiffer, K. W. Baldwin, K. W. West, D. Goldhaber-Gordon, and R. de Picciotto, Nat. Phys. **6**, 336–339 (2010).
[43]M. Kepenekian and J. Even, J. Phys. Chem. Lett. **8**, 3362 (2017).
[44]S. D. Stranks and P. Plochocka, Nat. Mater. **17**, 381–384 (2018).
[45]D. Giovanni, H. Ma, J. Chua, M. Grätzel, R. Ramesh, S. Mhaisalkar, N. Mathews, and T. C. Sum, Nano Lett. **15**, 1553–1558 (2015).
[46]D. Giovanni, W. K. Chong, H. A. Dewi, K. Thirumal, I. Neogi, R. Ramesh, S. Mhaisalkar, N. Mathews, and T. C. Sum, Sci. Adv. **2**, e1600477 (2016).
[47]B. Nafradi, P. Szirmai, M. Spina, H. Lee, O. V. Yazyev, A. Arakcheeva, D. Chernyshov, M. Gibert, L. Forró, and E. Horvath, Nat. Commun. **7**, 13406 (2016).
[48]V. V. Belykh, D. R. Yakovlev, M. M. Glazov, P. S. Grigoryev, M. Hussain, J. Rautert, D. N. Dirin, M. V. Kovalenko, and M. Bayer, Nat. Commun. **10**, 673 (2019).
[49]J. Wang, C. Zhang, H. Liu, R. McLaughlin, Y. Zhai, S. R. Vardeny, X. Liu, S. McGill, D. Semenov, H. Guo, R. Tsuchikawa, V. V. Deshpande, D. Sun, and Z. V. Vardeny, Nat. Commun. **10**, 129 (2019).
[50]M. Wang, H. Xu, T. Wu, H. Ambaye, J. Qin, J. Keum, I. N. Ivanov, V. Lauter, and B. Hu, Adv. Sci. **8**, 2004488 (2021).
[51]V. M. Edelstein, Solid State Commun. **73**, 233–235 (1990).
[52]M. I. Dyakonov and V. I. Perel, Phys. Lett. A **35**, 459 (1971).
[53]J. E. Hirsch, Phys. Rev. Lett. **83**, 1834 (1999).
[54]G. Dresselhaus, A. F. Kip, and C. Kittel, Phys. Rev. **95**, 568–569 (1954).
[55]P. Delugas, A. Filippetti, A. Gadaleta, I. Pallecchi, D. Marré, and V. Fiorentini, Phys. Rev. B **88**, 115304 (2013).
[56]K. Ishizaka, M. S. Bahramy, H. Murakawa, M. Sakano, T. Shimojima, T. Sonobe, K. Koizumi, S. Shin, H. Miyahara, A. Kimura, K. Miyamoto, T. Okuda, H. Namatame, M. Taniguchi, R. Arita, N. Nagaosa, K. Kobayashi, Y. Murakami, R. Kumai, Y. Kaneko, Y. Onose, and Y. Tokura, Nat. Mater. **10**, 521–526 (2011).
[57]D. Di Sante, P. Barone, R. Bertacco, and S. Picozzi, Adv. Mater. **25**, 509–513 (2013).
[58]P. D. C. King, R. C. Hatch, M. Bianchi, R. Ovsyannikov, C. Lupulescu, G. Landolt, B. Slomski, J. H. Dil, D. Guan, J. L. Mi, E. D. L. Rienks, J. Fink, A. Lindblad, S. Svensson, S. Bao, G. Balakrishnan, B. B. Iversen, J. Osterwalder, W. Eberhardt, F. Baumberger, and P. Hofmann, Phys. Rev. Lett. **107**, 096802 (2011).
[59]A. Varykhalov, D. Marchenko, M. R. Scholz, E. D. L. Rienks, T. K. Kim, G. Bihlmayer, J. Sanchez-Barriga, and O. Rader, Phys. Rev. Lett. **108**, 066804 (2012).
[60]C. R. Ast, J. Henk, A. Ernst, L. Moreschini, M. C. Falub, D. Pacilé, P. Bruno, K. Kern, and M. Grioni, Phys. Rev. Lett. **98**, 186807 (2007).
[61]Q. Liu, Y. Guo, and A. J. Freeman, Nano Lett. **13**, 5264 (2013).
[62]W. Yao, E. Wang, H. Huang, K. Deng, M. Yan, K. Zhang, K. Miyamoto, T. Okuda, L. Li, Y. Wang, H. Gao, C. Liu, W. Duan, and S. Zhou, Nat. Commun. **8**, 14216 (2017).
[63]M. A. U. Absor, I. Santoso, Harsojo, K. Abraha, H. Kotaka, F. Ishii, and M. Saito, Phys. Rev. B **97**, 205138 (2018).
[64]S. Sattar and J. A. Larsson, ACS Omega **6**, 4044 (2021).
[65]L. Xiang, Y. Ke, and Q. Zhang, Appl. Phys. Lett. **115**, 203501 (2019).
[66]J. Nitta, T. Akazaki, H. Takayanagi, and T. Enoki, Phys. Rev. Lett. **78**, 1335 (1997).
[67]H. Nakamura, T. Koga, and T. Kimura, Phys. Rev. Lett. **108**, 206601 (2012).
[68]A. D. Caviglia, M. Gabay, S. Gariglio, N. Reyren, C. Cancellieri, and J.-M. Triscone, Phys. Rev. Lett. **104**, 126803 (2010).
[69]A. Filippetti, P. Delugas, M. I. Saba, and A. Mattoni, J. Phys. Chem. Lett. **6**, 4909 (2015).
[70]X. Zhang, Q. Liu, J.-W. Luo, A. J. Freeman, and A. Zunger, Nat. Phys. **10**, 387–393 (2014).
[71]A. Mattoni, A. Filippetti, M. I. Saba, and P. Delugas, J. Phys. Chem. C **119**, 17421–17428 (2015).
[72]A. Mattoni, A. Filippetti, M. I. Saba, C. Caddeo, and P. Delugas, J. Phys. Chem. Lett. **7**, 529–535 (2016).
[73]A. Marronnier, G. Roma, M. A. Carignano, Y. Bonnassieux, C. Katan, J. Even, E. Mosconi, and F. De Angelis, J. Phys. Chem. C **123**, 291–298 (2019).
[74]S. McKechnie, J. M. Frost, D. Pashov, P. Azarhoosh, A. Walsh, and M. van Schilfgaarde, Phys. Rev. B **98**, 085108 (2018).
[75]M. Puppin, S. Polishchuk, N. Colonna, A. Crepaldi, D. N. Dirin, O. Nazarenko, R. De Gennaro, G. Gatti, S. Roth, T. Barillot, L. Poletto, R. P. Xian, L. Rettig, M. Wolf, R. Ernstorfer, M. V. Kovalenko, N. Marzari, M. Grioni, and M. Chergui, Phys. Rev. Lett. **124**, 206402 (2020).
[76]K. Frohna, T. Deshpande, J. Harter, W. Peng, B. A. Barker, J. B. Neaton, S. G. Louie, O. M. Bakr, D. Hsieh, and M. Bernardi, Nat. Commun. **9**, 1829 (2018).
[77]Z.-G. Yu, J. Phys. Chem. C **122**, 29607–29612 (2018).
[78]M. Sajedi, M. Krivenkov, D. Marchenko, A. Varykhalov, J. Sánchez-Barriga, E. D. L. Rienks, and O. Rader, Phys. Rev. B **102**, 081116(R) (2020).
[79]T. Komesu, X. Huang, T. R. Paudel, Y. B. Losovyj, X. Zhang, E. F. Schwier, Y. Kojima, M. Zheng, H. Iwasawa, K. Shimada, M. I. Saidaminov, D. Shi, A. L. Abdelhady, O. M. Bakr, S. Dong, E. Y. Tsymbal, and P. A. Dowben, J. Phys. Chem. C **120**, 21710–21715 (2016).
[80]C. Wang, B. R. Ecker, H. Wei, J. Huang, J.-Q. Mengc, and Y. Gao, Phys. Chem. Chem. Phys. **19**, 5361 (2017).
[81]M.-I. Lee, A. Barragán, M. N. Nair, V. L. R. Jacques, D. L. Bolloch, P. Fertey, K. Jemli, F. Lédée, G. Trippé-Allard, E. Deleporte, A. Taleb-Ibrahimi, and A. Tejeda, J. Phys. D **50**, 26LT02 (2017).

[82]J.-P. Yang, M. Meissner, T. Yamaguchi, X.-Y. Zhang, T. Ueba, L.-W. Cheng, S. Ideta, K. Tanaka, X.-H. Zeng, N. Ueno, and S. Kera, Sol. RRL **2**, 1800132 (2018).
[83]F. Zu, P. Amsalem, D. A. Egger, R. Wang, C. M. Wolff, H. Fang, M. A. Loi, D. Neher, L. Kronik, S. Duhm, and N. Koch, J. Phys. Chem. Lett. **10**, 601–609 (2019).
[84]D. Niesner, M. Hauck, S. Shrestha, I. Levchuk, G. J. Matt, A. Osvet, M. Batentschuk, C. Brabecc, H. B. Weber, and T. Fauster, Proc. Natl. Acad. Sci. U. S. A. **115**, 9509–9514 (2018).
[85]Z. Liu, C. Vaswani, X. Yang, X. Zhao, Y. Yao, Z. Song, D. Cheng, Y. Shi, L. Luo, D.-H. Mudiyanselage, C. Huang, J.-M. Park, R. H. J. Kim, J. Zhao, Y. Yan, K.-M. Ho, and J. Wang, Phys. Rev. Lett. **124**, 157401 (2020).
[86]E. Lafalce, E. Amerling, Z.-G. Yu, P. C. Sercel, L. Whittaker-Brooks, and Z. V. Vardeny, Nat. Commun. **13**, 483 (2022).
[87]Y. Liu, Y. Jiang, Z. Xu, L. Li, D. Zhang, W. Zheng, D. Liang, B. Zheng, H. Liu, X. Sun, C. Zhu, L. Lin, X. Zhu, H. Duan, Q. Yuan, X. Wang, S. Wang, D. Li, and A. Pan, Adv. Opt. Mater. **10**, 2200183 (2022).
[88]P. B. Allen, "Theory and resistivity of metals," in *Quantum Theory of Real Materials*, edited by J. R. Chelikowsky and S. G. Louie (Kluwer, Boston, 1996), pp. 219–250.
[89]G. Madsen and D. Singh, Comput. Phys. Commun. **175**, 67–71 (2006).
[90]S. D. Ganichev, E. L. Ivchenko, V. V. Belkov, S. A. Tarasenko, M. Sollinger, D. Weiss, W. Wegscheider, and W. Prettl, Nature **417**, 153–156 (2002).
[91]Y. Fan, P. Upadhyaya, X. Kou, M. Lang, S. Takei, Z. Wang, J. Tang, L. He, L.-T. Chang, M. Montazeri, G. Yu, W. Jiang, T. Nie, R. N. Schwartz, Y. Tserkovnyak, and K. L. Wang, Nat. Mater. **13**, 699–704 (2014).
[92]A. R. Mellnik, J. S. Lee, A. Richardella, J. L. Grab, P. J. Mintun, M. H. Fischer, A. Vaezi, A. Manchon, E. A. Kim, N. Samarth, and D. C. Ralph, Nature **511**, 449–453 (2014).
[93]K. Kondou, R. Yoshimi, A. Tsukazaki, Y. Fukuma, J. Matsuno, K. S. Takahashi, M. Kawasaki, Y. Tokura, and Y. Otani, Nat. Phys. **12**, 1027–1032 (2016).
[94]E. Lesne, Y. Fu, S. Oyarzun, J. C. Rojas-Sánchez, D. C. Vaz, H. Naganuma, G. Sicoli, J.-P. Attané, M. Jamet, E. Jacquet, J.-M. George, A. Barthélémy, H. Jaffrès, A. Fert, M. Bibes, and L. Vila, Nat. Mater. **15**, 1261 (2016).
[95]Q. Shao, G. Yu, Y.-W. Lan, Y. Shi, M.-Y. Li, C. Zheng, X. Zhu, L.-J. Li, P. K. Amiri, and K. L. Wang, Nano Lett. **16**, 7514–7520 (2016).
[96]T. S. Ghiasi, A. A. Kaverzin, P. J. Blah, and B. J. van Wees, Nano Lett. **19**, 5959–5966 (2019).
[97]R. Dey, A. Roy, L. F. Register, and S. K. Banerjee, APL Mater. **9**, 060702 (2021).
[98]R. Galceran, B. Tian, J. Li, F. Bonell, M. Jamet, C. Vergnaud, A. Marty, J. H. García, J. F. Sierra, M. V. Costache, S. Roche, S. O. Valenzuela, A. Manchon, X. Zhang, and U. Schwingenschlögl, APL Mater. **9**, 100901 (2021).
[99]T. Nan, C. D. Ralph, E. Y. Tsymbal, and A. Manchon, APL Mater. **9**, 120401 (2021).
[100]J. C. Rojas Sanchez, L. Vila, G. Desfonds, S. Gambarelli, J.-P. Attané, J. M. De Teresa, C. Magén, and A. Fert, Nat. Commun. **4**, 2944 (2013).
[101]J. C. Rojas-Sánchez, S. Oyarzún, Y. Fu, A. Marty, C. Vergnaud, S. Gambarelli, L. Vila, M. Jamet, Y. Ohtsubo, A. Taleb-Ibrahimi, P. Le Fèvre, F. Bertran, N. Reyren, J.-M. George, and A. Fert, Phys. Rev. Lett. **116**, 096602 (2016).
[102]Q. Song, H. Zhang, T. Su, W. Yuan, Y. Chen, W. Xing, J. Shi, J. Sun, and W. Han, Sci. Adv. **3**, e1602312 (2017).
[103]H. He, L. Tai, D. Wu, H. Wu, A. Razavi, K. Wong, Y. Liu, and K. L. Wang, APL Mater. **9**, 071104 (2021).
[104]L. Cheng, Z. Li, D. Zhao, and E. E. M. Chia, APL Mater. **9**, 070902 (2021).
[105]R. H. Silsbee, J. Phys.: Condens. Matter **16**, R179–R207 (2004).
[106]P. Gambardella and I. M. Miron, Philos. Trans. R. Soc. A **369**, 3175–3319 (2011).
[107]A. Filippetti, A. Mattoni, C. Caddeo, M. I. Saba, and P. Delugas, Phys. Chem. Chem. Phys. **18**, 15352–15362 (2016).
[108]A. D. Wright, C. Verdi, R. L. Milot, G. E. Eperon, M. A. Pérez-Osorio, H. J. Snaith, F. Giustino, M. B. Johnston, and L. M. Herz, Nat. Commun. **7**, 11755 (2016).
[109]M. Bokdam, T. Sander, A. Stroppa, S. Picozzi, D. D. Sarma, C. Franchini, and G. Kresse, Sci. Rep. **6**, 28618 (2016).
[110]M. Karakus, S. A. Jensen, F. D'Angelo, D. Turchinovich, M. Bonn, and E. Cánovas, J. Phys. Chem. Lett. **6**, 4991–4996 (2015).
[111]C. Motta, F. El-Mellouhi, and S. Sanvito, Sci. Rep. **5**, 12746 (2015).
[112]C. C. Stoumpos, C. D. Malliakas, and M. G. Kanatzidis, Inorg. Chem. **52**, 9019–9038 (2013).
[113]C. Wehrenfennig, G. E. Eperon, M. B. Johnston, H. J. Snaith, and L. M. Herz, Adv. Mater. **26**, 1584–1589 (2014).
[114]M. A. Pérez-Osorio, R. L. Milot, M. R. Filip, J. B. Patel, L. M. Herz, M. B. Johnston, and F. Giustino, J. Phys. Chem. C **119**, 25703–25718 (2015).
[115]S. Zhang and A. Fert, Phys. Rev. B **94**, 184423 (2016).
[116]D. Culcer, J. Sinova, N. A. Sinitsyn, T. Jungwirth, A. H. MacDonald, and Q. Niu, Phys. Rev. Lett. **93**, 046602 (2004).
[117]S.-Q. Shen, AAPPS Bull. **18**, 29–36 (2008).
[118]L. Camosi, J. Svetlík, M. V. Costache, W. S. Torres, I. F. Aguirre, V. Marinova, D. Dimitrov, M. Gospodinov, J. F. Sierra, and S. O. Valenzuela, 2D Mater. **9**, 035014 (2022).